

# Synergistic Promotion of Large-Current Water Splitting through Interfacial Engineering of Hierarchically Structured CoP–FeP Nanosheets with Rich P Vacancies

Luoluo Qi<sup>+</sup>,<sup>[a]</sup> Zhiyang Huang<sup>+</sup>,<sup>[a]</sup> Miao Liao,<sup>[a]</sup> Lei Wang,<sup>\*,[b]</sup> Lixia Wang,<sup>[a]</sup> Mingcheng Gao,<sup>[a]</sup> Tayirjan Taylor Isimjan,<sup>\*,[c]</sup> and Xiulin Yang<sup>\*,[a]</sup>

The development of hydrogen evolution reaction (HER) catalysts with high performance under large current density is still a challenge. Introducing P vacancies in heterostructure is an appealing strategy to enhance HER kinetics. This study investigates a CoP–FeP heterostructure catalyst with abundant P vacancies (Vp–CoP–FeP/NF) on nickel foam (NF), which was prepared using dipping and phosphating treatment. The optimized Vp–CoP–FeP catalyst exerted prominent HER catalytic capability, requiring an ultra-low overpotential (58 mV @ 10 mA cm<sup>-2</sup>) and displaying robust durability (50 h @ 200 mA cm<sup>-2</sup>) in 1.0 M KOH solution. Furthermore, the catalyst demonstrated superior overall water splitting activity as cath-

ode, demanding only cell voltage of 1.76 V at 200 mA cm<sup>-2</sup>, outperforming Pt/C/NF<sup>(-)</sup> || RuO<sub>2</sub>/NF<sup>(+)</sup>. The catalyst's outstanding performance can be attributed to the hierarchical structure of porous nanosheets, abundant P vacancies, and synergistic effect between CoP and FeP components, which promote water dissociation and H\* adsorption and desorption, thereby synergistically accelerating HER kinetics and enhancing HER activity. This study demonstrates the potential of HER catalysts with phosphorus-rich vacancies that can work under industrial-scale current density, highlighting the importance of developing durable and efficient catalysts for hydrogen production.

## Introduction

In light of the worldwide energy shortage and environmental pollution, questing clean, sustainable and pollution-free energy has become a critical strategic goal.<sup>[1]</sup> Among the promising energy carriers, hydrogen (H<sub>2</sub>) stands out due to its high energy density and zero-carbon emissions.<sup>[2]</sup> Electrochemical water splitting is considered as a feasible approach to generate H<sub>2</sub>.<sup>[3]</sup> Hydrogen evolution reaction (HER) kinetics, one of the half reactions of electrochemical water splitting, is two orders of magnitude slower in alkaline conditions than in acidic conditions.<sup>[4]</sup> Therefore, it is crucial to develop advanced and efficient HER electrocatalysts to accelerate alkaline HER kinetics.

Hitherto, while platinum (Pt) group metals (e.g., Pt, Pd and Ir) are identified as the most ideal HER catalysts, high cost and scarcity of noble metals greatly impede their large-scale commercial application.<sup>[5]</sup> In consequence, exploring alternative non-noble metal catalysts has garnered considerable attention, but remains a significant challenge.

Transition metal phosphides (TMPs) have gained attention as potential substitutes for Pt-group noble metals because of their unique catalytic mechanism and electronic structure.<sup>[6]</sup> Additionally, the lone pair electron in P 3p and unoccupied 3d orbitals can hybridize with other electrons of neighboring atoms, thereby modifying electron cloud density and promoting adsorption and desorption of intermediate H\*.<sup>[7]</sup> Among numerous TMPs, CoP–FeP is one of the most extensively studied. According to recent reports, HER catalytic capacity of CoP–FeP is ameliorated principally through morphological control, heterojunction construction and heteroatomic doping. For example, Wu et al. utilized nano-engineering strategy to modify active sites on a 3D porous substrate, achieving maximum exposure of the active sites and leading to the formation of an ultra-high electrochemically active surface area in the CoP@3DOM-FeP catalyst, thereby increasing mass transport for HER process.<sup>[8]</sup> Xu et al. reported that the introduction of Fe–Co–P multi-heterojunction can regulate the local electronic structure, leading to an improvement in the adsorption of reaction intermediates on active sites and thus enhancing catalytic performance.<sup>[9]</sup> Similarly, Lyu et al. demonstrated that interface effect between FeP and CoP can significantly adjust electronic structure of active sites, optimizing the adsorbed H<sub>ad</sub> free energy, and consequently, obtaining better catalytic activity.<sup>[10]</sup> Additionally, Zhang et al. utilized tungsten-doping to

[a] L. Qi,<sup>+</sup> Z. Huang,<sup>+</sup> M. Liao, L. Wang, M. Gao, Prof. Dr. X. Yang  
Guangxi Key Laboratory of Low Carbon Energy Materials  
School of Chemistry and Pharmaceutical Sciences  
Guangxi Normal University  
Guilin 541004 (China)  
E-mail: xlyang@gxnu.edu.cn

[b] Dr. L. Wang  
Department of Food and Environment Engineering  
Chuzhou Polytechnic  
Chuzhou 239000 (China)  
E-mail: stone@vip.qq.com

[c] Dr. T. Taylor Isimjan  
Saudi Arabia Basic Industries Corporation (SABIC) at  
King Abdullah University of Science and Technology (KAUST)  
Thuwal 23955-6900 (Saudi Arabia)  
E-mail: isimjant@sabic.com

[<sup>+</sup>] These authors contributed equally to this work.

Supporting information for this article is available on the WWW under <https://doi.org/10.1002/chem.202301521>

greatly improve the water adsorption capacity of FeCoP, and generate a special morphology conducive to mass transportation, which vastly enhances its HER activity.<sup>[11]</sup> However, there are few reports on the improvement of the catalytic performance of CoP–FeP by introducing P vacancies ( $P_v$ ). It is noteworthy that P vacancies can modulate electronic structure, improve electronic conductivity and optimize the intermediates adsorption energy for HER.<sup>[12]</sup>

Motivated by the aforementioned limitations and inspirations, we design and fabricate a CoP–FeP/NF heterostructure with abundant P vacancies ( $V_p$ -CoP–FeP/NF) through introducing interface engineering and phosphorus defects strategies. Multiple physical characterizations are applied to analyze the crystal structure, micro-morphology and chemical state. The results manifest that  $V_p$ -CoP–FeP/NF possesses plentiful P vacancies, strong electron interaction, large electrochemically active surface area and high conductivity, resulting in excellent alkaline HER performance. Specifically,  $V_p$ -CoP–FeP/NF delivers low overpotential of 58 mV at  $10 \text{ mA cm}^{-2}$  in 1.0 M KOH media and displays little activity decay after long-term durability and cycle stability tests. Moreover, it is also applied in a two-electrode water electrolysis device ( $\text{RuO}_2/\text{NF}^{(+)} \parallel V_p\text{-CoP-FeP}/\text{NF}$ ),

exhibiting excellent catalytic activity and robust long-term stability under high current density. Lastly, we propose a possible catalytic mechanism to explain the electrocatalytic water splitting for  $\text{H}_2$  production.

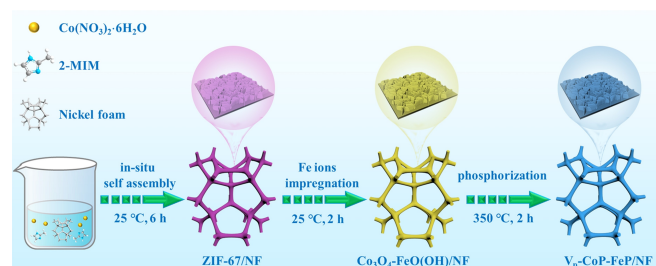
## Results and Discussion

### Structural and morphological characterizations

Scheme 1 outlined the synthesis process for  $V_p$ -CoP–FeP/NF. Firstly, ZIF-67 was self-assembled uniformly on the surface of NF by impregnation method. Subsequently, the obtained ZIF-67/NF was immersed in the  $\text{FeCl}_2$  solution for 2 h to produce  $\text{Co}_3\text{O}_4\text{-FeO(OH)}/\text{NF}$ . Finally, heterogeneous bimetallic phosphide  $V_p$ -CoP–FeP/NF was fabricated by low-temperature phosphorization. During the synthesis process, the color of the catalyst changed from purple to brownish yellow, and finally turned black (Figure S2).

X-ray diffraction (XRD) was used to elucidate crystallographic structure of resultant catalysts. Figure S3a showed that XRD pattern of as-prepared ZIF-67/NF matched well with that of the simulated ZIF-67.<sup>[13]</sup> Upon being immersed in the  $\text{FeCl}_2$  solution for 2 h, ZIF-67/NF transformed into mixed phases of  $\text{Co}_3\text{O}_4$  (JCPDS: 42-1467) and  $\text{FeO(OH)}$  (JCPDS: 08-0098) (Figure S3b).<sup>[14]</sup> Finally, after low-temperature phosphating treatment, the primary peaks of catalyst ( $V_p$ -CoP–FeP/NF) corresponded well to CoP (JCPDS: 29-0497) and FeP (JCPDS: 39-0809) phases (Figure 1a).<sup>[15]</sup> The CoP/NF, FeP/NF and CoP–FeP/NF were also synthesized as the controls (Figure S4).

The morphology of  $V_p$ -CoP–FeP/NF was examined using scanning electron microscopy (SEM). As presented in Figure S5a, ZIF-67/NF exhibited smooth nanosheets with an average thickness of 150 nm, staggered and tightly coupled on



Scheme 1. Schematic diagram of synthesis of  $V_p$ -CoP–FeP/NF.

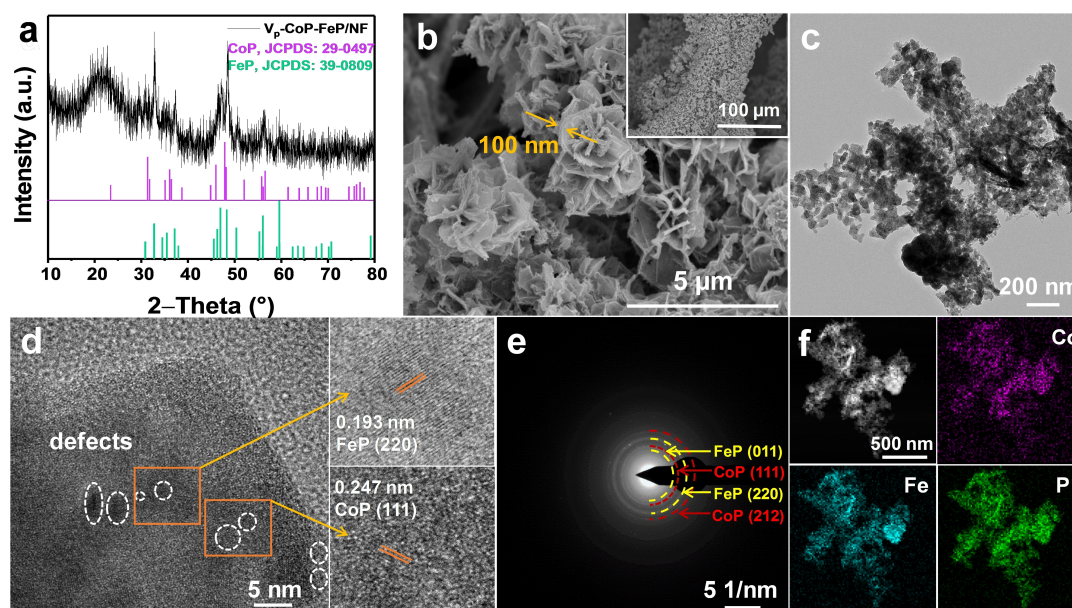
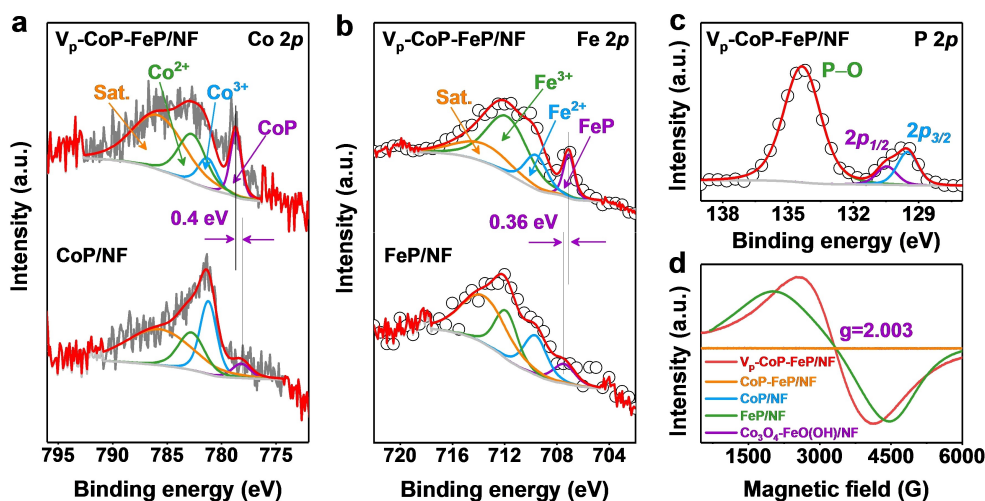


Figure 1. (a) XRD pattern, (b) SEM image, (c) TEM image, (d) HR-TEM image, (e) SAED image and (f) HAADF-STEM image and elemental mapping images of  $V_p$ -CoP–FeP/NF.

the NF. Accompanied by impregnation of iron (Fe) ions, the morphology of  $\text{Co}_3\text{O}_4\text{-FeO(OH)/NF}$  changed to hierarchical structure comprised of numerous nanosheets (Figure S5b).<sup>[16]</sup> Following gas phosphating, the morphology remained unchanged (Figure 1b). Notably, the average thickness of nanosheets was thinned from 150 nm to 100 nm, which was conducive to charge transfer, ion transport and gas release.<sup>[17]</sup> In contrast,  $\text{CoP/NF}$  and  $\text{FeP/NF}$  exhibited closely aligned nanosheets with significant aggregation (Figure S6). Furthermore, SEM images of  $\text{Vp-CoP-FeP/NF-x}$  ( $x = 1 \text{ h, 4 h, 8 h}$ ) were seen in Figure S7. As the impregnation time increased, the spacing between nanosheets became smaller and the distribution became denser. Consequently, reasonable impregnation time was beneficial to the formation of hierarchical structure composed of nanosheets, exposing abundant active sites and accelerating mass transfer. The microstructure of  $\text{Vp-CoP-FeP/NF}$  was further investigated by transmission electron microscopy (TEM). TEM image in Figure 1c confirmed that  $\text{Vp-CoP-FeP/NF}$  displayed porous nanosheets structure that was advantageous for enriching active sites, facilitating ion transport, and enhancing electrocatalytic activity.<sup>[18]</sup> As viewed in Figure 1d, the high-resolution TEM (HR-TEM) image exhibited lattice spacings of 0.193 nm and 0.247 nm, corresponding to (220) and (111) crystal planes of orthorhombic FeP and orthorhombic CoP, respectively. Notably, many discontinuous points (marked with white dashed circles) in the HR-TEM image of  $\text{Vp-CoP-FeP/NF}$  manifest the presence of plentiful vacancies.<sup>[19]</sup> Besides, the diffraction rings in the selected area electron diffraction (SAED) pattern revealed the characteristic crystal planes of orthorhombic FeP and CoP (Figure 1e). Meanwhile, porous nanosheets structure of  $\text{Vp-CoP-FeP/NF}$  was further revealed by high-angle annular dark-field scanning transmission electron microscopy (HAADF-STEM). And corresponding element mappings demonstrated that elements Co, Fe and P were evenly distributed in  $\text{Vp-CoP-FeP/NF}$  (Figure 1f and Figure S8). Additionally, the surface area and pore size of  $\text{Vp-CoP-FeP/NF}$  were measured by  $\text{N}_2$  adsorption-desorption

isotherm analysis. As displayed in Figure S9, the Brunauer-Emmett-Teller (BET) specific surface area of  $\text{Vp-CoP-FeP/NF}$  was determined to be  $22.56 \text{ m}^2 \text{ g}^{-1}$  and the average pore diameter was approximately 38.92 nm.

X-ray photoelectron spectroscopy (XPS) was implemented to investigate elemental composition and surface chemical valence states of catalysts. XPS survey spectra revealed the presence of C, O, P, Fe and Co elements in  $\text{Vp-CoP-FeP/NF}$  (Figure S10a). The high-resolution C 1s spectrum of  $\text{Vp-CoP-FeP/NF}$  was deconvoluted into C=C (284.0 eV), C-C (284.8 eV), C-O or C=N (286.0 eV) and C=O (289.0 eV) (Figure S10b).<sup>[20]</sup> As viewed in Figure 2a, the Co  $2p_{3/2}$  region of  $\text{Vp-CoP-FeP/NF}$  was deconvoluted into four peaks, matching with Co-P (778.7 eV),  $\text{Co}^{3+}$  (781.3 eV),  $\text{Co}^{2+}$  (782.7 eV) and satellite peak (785.8 eV).<sup>[21]</sup> Compared with  $\text{CoP/NF}$ , the  $\text{Co}^{2+}/\text{Co}^{3+}$  ratio of  $\text{Vp-CoP-FeP/NF}$  increased due to the introduction of reductive FeP, which made  $\text{Co}^{3+}$  be reduced to  $\text{Co}^{2+}$ .<sup>[22]</sup> Additionally, the addition of FeP could change the electronic structure of CoP, promote the combination of Co and P and the electron transport rate between Co and P, thereby forming a more stable Co-P chemical bond and enhancing the peak of Co-P.<sup>[23]</sup> The binding energy of Co-P of  $\text{Vp-CoP-FeP/NF}$  relative to  $\text{CoP/NF}$  was positively shifted by 0.40 eV. Moreover, the Fe  $2p_{3/2}$  region of  $\text{Vp-CoP-FeP/NF}$  was divided into four peaks, which were assigned to Fe-P (707.1 eV),  $\text{Fe}^{2+}$  (709.6 eV),  $\text{Fe}^{3+}$  (711.8 eV) and satellite peak (713.7 eV) (Figure 2b).<sup>[24]</sup> Comparing with  $\text{FeP/NF}$ , the binding energy of Fe-P of  $\text{Vp-CoP-FeP/NF}$  was negatively shifted by 0.36 eV. The apparent shifts in binding energy testified that the charge transferred from CoP to FeP, forming electron-deficient CoP and electron-rich FeP, accounting for intense electron interaction between CoP and FeP species.<sup>[10]</sup> The strong electron interaction can accelerate charge transfer, improve electron conductivity, regulate electronic structure on the interface and optimize the adsorption energies of reaction intermediates, which is in favor of the dissociation of water and the adsorption and desorption of hydrogen, thus enhancing catalytic performance.<sup>[9-10,25]</sup> Mean-



**Figure 2.** High-resolution XPS spectra of (a) Co  $2p$ , (b) Fe  $2p$  and (c) P  $2p$  of  $\text{Vp-CoP-FeP/NF}$  and (d) EPR spectra of  $\text{Vp-CoP-FeP/NF}$ ,  $\text{CoP-FeP/NF}$ ,  $\text{CoP/NF}$ ,  $\text{FeP/NF}$  and  $\text{Co}_3\text{O}_4\text{-FeO(OH)/NF}$ .

while, the P 2p region was fitted to three peaks, corresponding to P 2p<sub>1/2</sub> (130.5 eV) and P 2p<sub>3/2</sub> (129.5 eV) for P–Co or P–Fe as well as P–O bonds (134.4 eV) (Figure 2c).<sup>[26]</sup> In addition, the effect of phosphating treatment on phosphorus atom coordination was investigated using electron paramagnetic resonance (EPR). As presented in Figure 2d, V<sub>p</sub>–CoP–FeP/NF performed the strongest EPR signal around g=2.003,<sup>[27]</sup> while no EPR signal appeared in Co<sub>3</sub>O<sub>4</sub>–FeO(OH)/NF, confirming the presence of P vacancies, identifying the classification of defects in the HR-TEM and revealing that phosphating treatment was capable of inducing the formation of phosphorus vacancies.<sup>[28]</sup> Specifically, the introduced P vacancies could modulate the electronic structure, improve the intrinsic conductivity and enhance the reaction kinetics.<sup>[28]</sup>

### Electrochemical HER performance

The HER performance of different catalysts was investigated in a standard three-electrode system in 1.0 M KOH. By altering dipping time of Fe ions, the catalytic performance was made

superior (Figure S11–12 and Table S2). It was observed that the catalyst exhibited the best catalytic performance when the dipping time was 2 h. Therefore, unless explicitly stated otherwise, V<sub>p</sub>–CoP–FeP/NF discussed below was acquired under the optimum synthesis conditions. Similarly, V<sub>p</sub>–CoP–FeP/NF had the optimal catalytic activity comparing with CoP–FeP/NF, Co<sub>3</sub>O<sub>4</sub>–FeO(OH)/NF and ZIF-67/NF (Figure S13–14 and Table S3), manifesting P vacancies play an essential role in improving HER activity.

For comparison, CoP/NF, FeP/NF and Pt/C/NF were also measured under identical conditions. As displayed in Figure 3a–b, V<sub>p</sub>–CoP–FeP/NF delivered extraordinary HER performance with ultralow overpotentials of 58 and 144 mV at 10 and 100 mA cm<sup>-2</sup>, superior to CoP/NF ( $\eta_{10}$ =91 mV,  $\eta_{100}$ =182 mV) and FeP/NF ( $\eta_{10}$ =159 mV,  $\eta_{100}$ =318 mV), illustrating that the introduction of Fe ions could enhance catalytic activity,<sup>[9]</sup> and there was strong interaction between CoP and FeP.<sup>[29]</sup> Notably, V<sub>p</sub>–CoP–FeP/NF surpassed Pt/C/NF when the current density exceeded 50 mA cm<sup>-2</sup>. The Tafel slope was applied to examine HER kinetics mechanism.<sup>[30]</sup> In Figure 3c, the Tafel slope of V<sub>p</sub>–CoP–FeP/NF (70.6 mV dec<sup>-1</sup>) was lower than other catalysts,

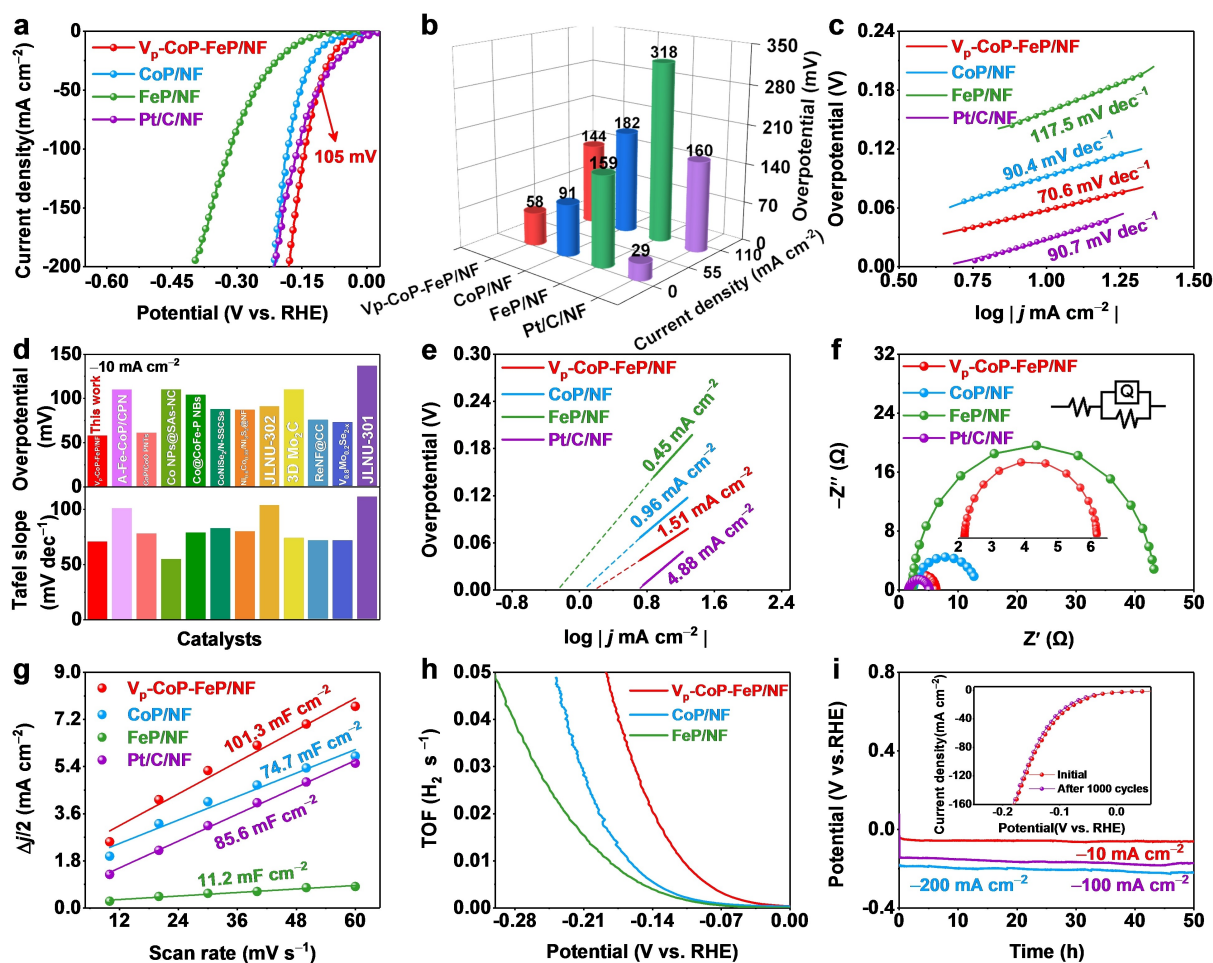


**Figure 3.** HER performance of V<sub>p</sub>–CoP–FeP/NF, CoP/NF, FeP/NF, and Pt/C/NF in 1.0 M KOH. (a) LSV polarization curves, (b) comparison of overpotentials at 10 and 100 mA cm<sup>-2</sup>, (c) Tafel slopes, (d) comparison of overpotential and Tafel slope with recently reported catalysts, (e) exchange current density ( $j_0$ ), (f) Nyquist plots, (g) double-layer capacitance ( $C_{dl}$ ), (h) turnover frequency (TOF) curves and (i) durability test of V<sub>p</sub>–CoP–FeP/NF (inset: LSV polarization curves of V<sub>p</sub>–CoP–FeP/NF before and after 1000 cycles).

demonstrating that Vp–CoP–FeP/NF had more favorable reaction kinetics and followed Volmer–Heyrovsky reaction pathway ( $\text{H}_2\text{O} + \text{e}^- = \text{H}_{\text{ad}} + \text{OH}^-$  and  $\text{H}_{\text{ad}} + \text{H}_2\text{O} + \text{e}^- = \text{H}_2\uparrow + \text{OH}^-$ ).<sup>[31]</sup> Moreover, HER performance of Vp–CoP–FeP/NF was more significant than that of most recently reported catalysts (Figure 3d and Table S4). As shown in Figure 3e, exchange current density ( $j_0$ ) was obtained by extrapolating Tafel slope to measure intrinsic HER catalytic activity of materials.<sup>[32]</sup> The  $j_0$  value of Vp–CoP–FeP/NF ( $1.51 \text{ mA cm}^{-2}$ ) was higher than that of other comparative catalysts except Pt/C/NF, indicating that Vp–CoP–FeP/NF can make electrode reaction easier and electron transfer faster. The Nyquist plots (Figure 3f) showed that Vp–CoP–FeP/NF had smaller charge-transfer resistance ( $R_{\text{ct}}$ ) approaching that of Pt/C/NF, revealing its stronger electron transfer capability, higher conductivity and faster reaction kinetics.<sup>[33]</sup> To further determine the source of outstanding HER performance, electrochemically active surface area (ECSA) of the catalyst was estimated by measuring the double-layer capacitance ( $C_{\text{dl}}$ ) (Figure 3g and Figure S15–16).<sup>[34]</sup> The values of  $C_{\text{dl}}$  and ECSA of Vp–CoP–FeP/NF ( $101.3 \text{ mF cm}^{-2}$ ,  $2532.5 \text{ cm}^2$ ) were larger than CoP/NF ( $74.7 \text{ mF cm}^{-2}$ ,  $1867.5 \text{ cm}^2$ ), FeP/NF ( $11.2 \text{ mF cm}^{-2}$ ,  $280 \text{ cm}^2$ ) and Pt/C/NF ( $85.6 \text{ mF cm}^{-2}$ ,  $2140.0 \text{ cm}^2$ ), which illustrated that Vp–CoP–FeP/NF could expose more active sites to enhance the HER performance.<sup>[35]</sup> Similarly, the value of  $C_{\text{dl}}$  of Vp–CoP–FeP/NF was larger than that of Co/Fe-based catalysts recently published (Figure S17 and Table S5). Meanwhile, turnover frequency (TOF) calculated from ICP-MS result (Table S1) was dedicated to estimate intrinsic catalytic activity of catalysts.<sup>[36]</sup> Figure 3h demonstrated that the TOF value of each catalyst increased monotonically with increasing potential and Vp–CoP–FeP/NF possessed the highest TOF value at the same potential, reflecting its high HER conversion efficiency and strong intrinsic catalytic activity.<sup>[37]</sup> The electrochemical durability of Vp–CoP–FeP/NF was detected through chronopotentiometry (CP) and CV tests (Figure 3i). The result revealed that there was almost no increase in overpotential at 10, 100 and 200  $\text{mA cm}^{-2}$  for 50 h, which illustrated the strong endurance of Vp–CoP–FeP/NF, especially at high current density.<sup>[38]</sup> Additionally, HER performance of Vp–CoP–FeP/NF showed little deterioration after 1000 cycles of CV scans, further proving superior stability.<sup>[39]</sup> SEM and XPS were used to characterize the morphology and chemical structure of the catalyst after long-term stability testing. The results indicated that the morphology and structure of the catalyst remained nanosheets, and XPS spectra showed that Vp–CoP–FeP/NF maintained its original chemical state, demonstrating its prominent stability for HER (Figure S18–19).<sup>[40]</sup>

### Mechanism analysis

The work function (WF) value determines the direction and possibility of electron transfer, which describes the driving factor and the balance effect.<sup>[41]</sup> The difference in WF values between CoP (5.06 eV) and FeP (5.13 eV) signifies that electrons transfer from CoP to FeP at the interface, resulting in electron-deficient CoP and electron-rich FeP, as indicated by the XPS

analysis, which makes it favorable towards water dissociation on CoP species and  $\text{H}^*$  adsorption and desorption on FeP species.<sup>[42]</sup> DFT calculation by Lyu et al. have shown that Gibbs free energy of hydrogen ( $\Delta G_{\text{H}^*}$ ) of FeP ( $-0.18 \text{ eV}$ ) is close to 0 than that of CoP (0.26 eV), indicating that FeP is conducive to adsorption and desorption of hydrogen<sup>[10]</sup>. Li et al. and Zhang et al. have demonstrated that CoP (0.05 eV) possesses lower water dissociation barrier ( $\Delta E_{\text{w}}$ ) compared to FeP (0.41 eV), indicating that CoP is more competitive for water dissociation.<sup>[43]</sup> Therefore, based on these findings, the alkaline HER mechanism of Vp–CoP–FeP/NF was proposed in Figure 4. Firstly, electron-deficient CoP absorbs  $\text{H}_2\text{O}$  molecule and then forms a transition state (TS) intermediate. At this point, more charge is transferred from  $\text{H}_2\text{O}$  to the CoP, and the O–H bond of the  $\text{H}_2\text{O}$  molecule can be weakened, thus facilitating  $\text{H}_2\text{O}$  dissociation. Secondly, the  $\text{H}_2\text{O}$  molecule is dissociated into the adsorbed  $\text{H}^*$  and  $\text{OH}^*$  at the interface. Thirdly, the adsorbed  $\text{OH}^*$  combines with an electron and then generates  $\text{OH}^-$  on the CoP. Eventually, the formed  $\text{H}^*$  on the FeP combines with another electron and  $\text{H}_2\text{O}$  molecule, simultaneously releasing  $\text{H}_2$  and creating new active site for the next cycle. Additionally, it should be noted that the presences of abundant P vacancies and strong electron interaction between CoP and FeP are conducive to facilitating the charge transfer, accelerating adsorption and dissociation of active intermediates at the interface, and providing suitable adsorption energy for reaction intermediates.<sup>[44]</sup>

### Overall water splitting analysis

The above mentioned experiments demonstrated that Vp–CoP–FeP/NF was a high-efficiency and stable HER electrocatalyst. Therefore, Vp–CoP–FeP/NF and  $\text{RuO}_2/\text{NF}$  were employed to the respective cathode and anode to assemble a two-electrode system for appraising the feasibility for overall water splitting of Vp–CoP–FeP/NF (Figure 5a). As a reference, Pt/C/NF was also tested as cathode. The cell voltages of  $\text{RuO}_2/\text{NF}^{(+)} \parallel \text{Vp-CoP-FeP/NF}^{(-)}$  were 1.58 and 1.72 V at 10 and 100  $\text{mA cm}^{-2}$ ,

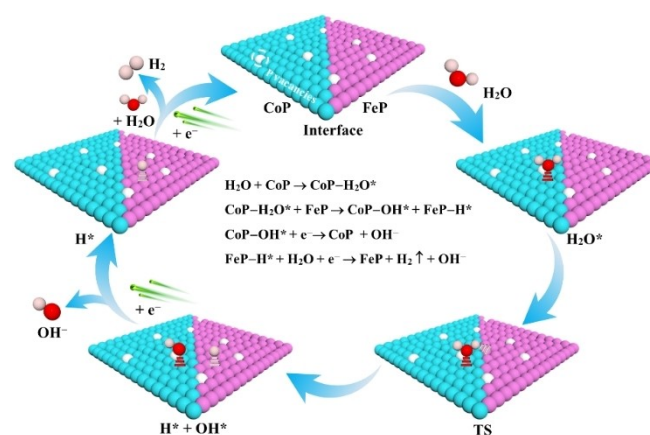


**Figure 4.** HER mechanism of Vp–CoP–FeP/NF catalyst in alkaline medium (the purple, indigo and white balls represent FeP, CoP and P vacancies, respectively).

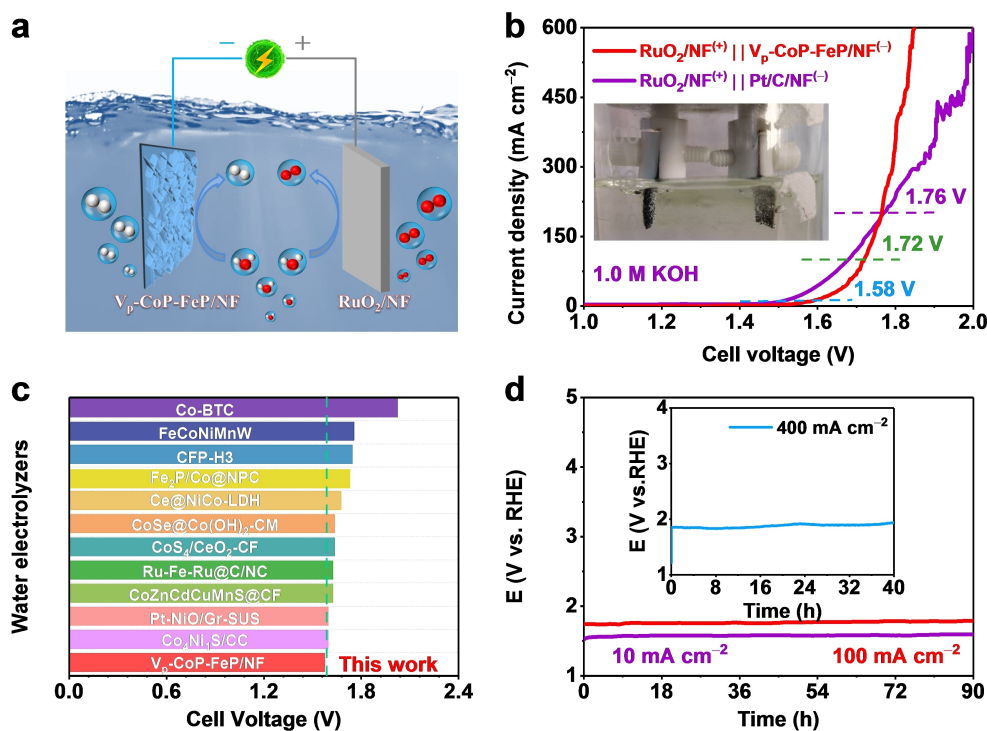


**Figure 5.** (a) Schematic diagram of overall water splitting in a two-electrode system, (b) LSV polarization curves of  $\text{RuO}_2/\text{NF}^{(+)} \parallel \text{V}_p\text{-CoP-FeP/NF}^{(-)}$  and  $\text{RuO}_2/\text{NF}^{(+)} \parallel \text{Pt/C/NF}^{(-)}$  for overall water splitting in 1.0 M KOH, (c) comparison of cell voltages between  $\text{RuO}_2/\text{NF}^{(+)} \parallel \text{V}_p\text{-CoP-FeP/NF}^{(-)}$  and other electrocatalysts reported in literatures and (d) durability test of  $\text{RuO}_2/\text{NF}^{(+)} \parallel \text{V}_p\text{-CoP-FeP/NF}^{(-)}$  at 10, 100 and 400  $\text{mA cm}^{-2}$ .

lower than that of most electrocatalysts reported recently and slightly higher than  $\text{RuO}_2/\text{NF}^{(+)} \parallel \text{Pt/C/NF}^{(-)}$ . However, its performance (1.76 V @ 200  $\text{mA cm}^{-2}$ ) exceeded  $\text{RuO}_2/\text{NF}^{(+)} \parallel \text{Pt/C/NF}^{(-)}$  at high current density (Figure 5b–c and Table S6), which is because the drip-coated powder Pt/C on NF is falling off more easily, the active sites being buried, slower mass transfer at high current density.<sup>[45]</sup> As exhibited in Figure 5d, the  $\text{RuO}_2/\text{NF}^{(+)} \parallel \text{V}_p\text{-CoP-FeP/NF}^{(-)}$  could stably operate for 90 h at 10 and 100  $\text{mA cm}^{-2}$ , and even 40 h at 400  $\text{mA cm}^{-2}$ , with almost no decline in performance, implying that  $\text{RuO}_2/\text{NF}^{(+)} \parallel \text{V}_p\text{-CoP-FeP/NF}^{(-)}$  had great potential for practical application at either high or low current density. In addition, there was continuous production of hydrogen and oxygen at both cathode and anode of the two-electrode configuration, meaning that the system possessed outstanding stability and industrial application prospect.

The superior HER performance of  $\text{V}_p\text{-CoP-FeP/NF}$  was ascribed to the following reasons: (1) In-situ synthesized self-supporting electrodes can reduce resistance and promote electron diffusion. (2) The hierarchical structure composed of porous nanosheets facilitates exposure of active sites, ion transport and gas release. (3) Phosphorus vacancies can improve conductivity, facilitating charge transfer. (4) The strong synergy between CoP and FeP, along with rich P vacancies can promote the dissociation of water and desorption of hydrogen, thereby reducing reaction energy barrier and promoting HER performance and kinetics.

## Conclusions

In summary, heterogeneous CoP–FeP/NF with abundant P vacancies ( $\text{V}_p\text{-CoP-FeP/NF}$ ) was successfully synthesized by impregnation and gas phosphating treatment. Benefiting from unique hierarchical structure, plentiful P vacancies and intense electron interaction,  $\text{V}_p\text{-CoP-FeP/NF}$  delivers glorious HER performance with low overpotential of 58 mV at 10  $\text{mA cm}^{-2}$ , low Tafel slope of 70.6  $\text{mV dec}^{-1}$ , small charge transfer resistance of 3.8  $\Omega$ , large electrochemically active surface area of 2532.5  $\text{cm}^2$ , and excellent durability. Furthermore, the cell voltage of  $\text{V}_p\text{-CoP-FeP/NF}$ -based electrolyzer is equivalent to that of the commercial Pt/C-based electrolyzer at 200  $\text{mA cm}^{-2}$ , manifesting promising commercial application prospect. This work offers a practical strategy using P vacancies and interfacial effect to boost synergistically water dissociation and hydrogen desorption, thereby improving HER activity.

## Experimental Section

**Chemicals and materials:** The chemicals and materials used in this experiment were purchased from various suppliers. Cobalt (II) nitrate hexahydrate ( $\text{Co}(\text{NO}_3)_2 \cdot 6\text{H}_2\text{O}$ , 99%), 2-methyl-imidazole ( $\text{C}_4\text{H}_6\text{N}_2$ , 98%), iron (II) chloride ( $\text{FeCl}_2$ , 99.5%) and sodium hypophosphite monohydrate ( $\text{NaH}_2\text{PO}_2 \cdot \text{H}_2\text{O}$ , 99%) were purchased from Shanghai Aladdin Biochemical Technology Co., LTD. Absolute ethanol ( $\text{C}_2\text{H}_5\text{OH}$ ,  $\geq 99.7\%$ ) and sulfuric acid ( $\text{H}_2\text{SO}_4$ ) were obtained from Xilong Chemical Reagent Co., LTD. Potassium hydroxide (KOH, 90%) was acquired from Shanghai Macklin Biochemical Technology

Co., LTD. Commercial Pt/C (20 wt.%) was got from Alfa Aesar. All chemical reagents were analytical grade and were used without further purification. The nickel foam (NF) with the dimension of 400 mm × 400 mm and thickness of 1.6 mm was acquired from Kunshan Longshengbao Electronic Materials Co., LTD.

**Synthesis of ZIF-67/NF:** To begin the experiment, a piece of NF (1 cm × 1 cm) was sonicated adequately with 0.5 M H<sub>2</sub>SO<sub>4</sub>, ethanol and deionized (DI) water for 10 min each. Next, 1.6 mmol of Co(NO<sub>3</sub>)<sub>2</sub>·6H<sub>2</sub>O and 8.0 mmol of 2-methylimidazole (2-MIM) were severally dissolved in 20 mL of DI water, stirred for 5 min and labeled as solutions A and B, respectively. Solution B was then added to solution A and stirred continuously to form a uniform mixture. After stirring for 5 min, the pretreated NF was placed vertically into the above mixture and allowed sitting for 6 h. Finally, the resulting material, ZIF-67 modified NF (named as ZIF-67/NF), was taken out, washed with DI water, and left to dry naturally at room temperature.

**Synthesis of Co<sub>3</sub>O<sub>4</sub>-FeO(OH)/NF-x:** The Co<sub>3</sub>O<sub>4</sub>-FeO(OH)/NF was prepared using dipping method. Firstly, 1.0 mmol of FeCl<sub>2</sub> was dissolved in 10 mL of DI water and sonicated to create homogeneous solution. Then, ZIF-67/NF was submerged in the above solution for 2 h. After 2 h of reaction, the product was rinsed with DI water and dried at room temperature. According to different dipping time, the samples were designated as Co<sub>3</sub>O<sub>4</sub>-FeO(OH)/NF-x (x = 1 h, 2 h, 4 h, 8 h).

**Synthesis of Vp-CoP-FeP/NF-x:** The Co<sub>3</sub>O<sub>4</sub>-FeO(OH)/NF-x and 1.0 g NaH<sub>2</sub>PO<sub>2</sub>·H<sub>2</sub>O were placed in the downstream and upstream porcelain boats in the tube furnace, respectively. Whereafter, the tube furnace was heated to 350 °C for 2 h at a rate of 5 °C min<sup>-1</sup> under the protection of nitrogen (N<sub>2</sub>). When the tube furnace was cooled to room temperature, the prepared samples were removed and named as Vp-CoP-FeP/NF-x. For the comparison study, CoP/NF, FeP/NF and CoP-FeP were synthesized, as described in the Supporting Information.

**Synthesis of Pt/C/NF and RuO<sub>2</sub>/NF:** The RuO<sub>2</sub> powder was prepared by direct calcination of RuCl<sub>3</sub>·3H<sub>2</sub>O in the tube furnace that was heated to 400 °C for 3 h in air. Then, 2.0 mg commercial Pt/C or RuO<sub>2</sub> was dispersed ultrasonically in the mixture of 200 μL ethanol, 200 μL DI water and 10 μL 5 wt.% Nafion for 30 min to form a uniform ink. Finally, the ink was pipetted onto the surface of NF (1 cm × 1 cm) and dried spontaneously in air to obtain the benchmark catalyst Pt/C/NF or RuO<sub>2</sub>/NF.

**Electrochemical measurements:** The electrochemical hydrogen evolution performance of different samples was monitored on Biologic VMP3 multichannel electrochemical workstation utilizing a conventional three-electrode system in 1.0 M KOH. Among them, the prepared electrocatalysts, carbon rod and saturated calomel electrode (SCE) were treated as working, counter and reference electrode, respectively. The measured potential ( $E_{SCE}$ ) was converted to the reversible hydrogen potential ( $E_{RHE}$ ) according to the equation of  $E_{RHE} = E_{SCE} + 0.241 + 0.059 \times \text{pH}$  (Figure S1). The pH value of freshly prepared 1.0 M KOH solution was 13.54 as measured by a pH meter. In the process of testing, the synthesized catalysts were preactivated to reach a steady state by performing electrochemical cyclic voltammetry (CV) tests at a scan rate of 5 mV s<sup>-1</sup> for several cycles. The linear sweep voltammetry (LSV) measurements were carried out to investigate HER performance of materials at a scan rate of 2 mV s<sup>-1</sup>. Electrochemical impedance spectroscopy (EIS) was proceeded in the frequent range from 200 kHz to 10 mHz to evaluate electron transfer ability. The double-layer capacitance ( $C_{dl}$ ) was studied by performing CV measurements within non-Faradaic potential window and at different scan rates (10–60 mV s<sup>-1</sup>). The long-term durability of the catalyst was ex-

plored by chronopotentiometry (CP). The stability of the catalyst was evaluated by cycling stability. Overall water splitting was conducted in a standard two-electrode system with a scan rate of 0.5 mV s<sup>-1</sup> in 1.0 M KOH. All curves in this work were rectified through *iR* compensation, and every electrochemical test was performed at room temperature (25 ± 1 °C).

**Material characterizations:** The crystal constructions of the materials were analyzed by the collected X-ray powder diffraction (XRD) data that was obtained by using a D/Max 2500 V/PC diffractometer with Cu K $\alpha$  radiation (Rigaku, Japan). The morphology and microstructure of the catalysts were investigated by the field emission environmental scanning electron microscope (SEM, Quanta 200 FEG, Holland) and transmission electron microscope (TEM, JEOL, JEM-2100F). The elemental composition and chemical valence states on the surface of the catalysts were analyzed through X-ray photoelectron spectrometer (XPS, JPS-9010TR, Japan). The actual contents of metallic elements in the materials were detected by inductively coupled plasma mass spectrometer (ICP-MS). The specific surface area, pore size distribution and nitrogen adsorption-desorption isotherm of the catalyst were calculated by Brunauer-Emmett-Teller (BET, 3H-2000PS4, BeiShiDe Instrument) and Barrett-Joyner-Halenda (BJH) method. The presence and intensity of phosphorus vacancies in the catalysts were measured by the electron paramagnetic resonance spectrometer (EPR, Bruker A300, Germany).

## Supporting Information

Additional references cited within the Supporting Information.<sup>[31a,40,46]</sup>

## Acknowledgements

This work has been supported by the National Natural Science Foundation of China (no. 21965005), Natural Science Foundation of Guangxi Province (2021GXNSFAA076001), Project of High-Level Talents of Guangxi (F-KA18015), and Guangxi Technology Base and Talent Subject (GUIKE AD20297039, GUIKE AD18126001).

## Conflict of Interests

The authors declare no conflict of interest.

## Data Availability Statement

Research data are not shared.

**Keywords:** CoP-FeP · hydrogen evolution · overall water splitting · phosphorus vacancy · synergistic effect

- [1] a) F. Liu, C. Shi, X. Guo, Z. He, L. Pan, Z. F. Huang, X. Zhang, J. J. Zou, *Adv. Sci.* **2022**, *9*, 2200307; b) K. Sun, Y. Q. Zhao, J. Yin, J. Jin, H. W. Liu, P. X. Xi, *Acta Phys.-Chim. Sin.* **2022**, *38*, 2107005.

- [2] a) A. Mondal, A. Vomiero, *Adv. Funct. Mater.* **2022**, *32*, 2208994; b) S. R. Xu, Q. Wu, B. A. Lu, T. Tang, J. N. Zhang, J. S. Hu, *Acta Phys. -Chim. Sin.* **2023**, *39*, 2209001.
- [3] a) S. Yan, W. Y. Liao, M. X. Zhong, W. M. Li, C. Wang, N. Pinna, W. Chen, X. F. Lu, *Appl. Catal. B* **2022**, *307*, 121199; b) A. Q. Wang, J. Chen, P. F. Zhang, S. Tang, Z. C. Feng, T. T. Yao, C. Li, *Acta Phys -Chim. Sin.* **2023**, *39*, 2301023.
- [4] Y. Hu, H. Yu, L. Qi, J. Dong, P. Yan, T. Taylor Isimjan, X. Yang, *ChemSusChem* **2021**, *14*, 1565–1573.
- [5] M. C. Liu, Z. P. Lei, Q. P. Ke, P. X. Cui, J. C. Wang, J. C. Yan, Z. K. Li, H. F. Shui, S. B. Ren, Z. C. Wang, Y. Kong, S. G. Kang, *Carbon Energy* **2022**, *4*, 480–490.
- [6] a) G. Yilmaz, T. Yang, K. J. H. Lim, S. W. Chee, L. Shen, U. Mirsaidov, M. Bosman, G. W. Ho, *EcoMat* **2022**, *5*, e12312; b) S. F. Yang, X. B. Yang, Q. Wang, X. Q. Cui, H. B. Zou, X. L. Tong, N. J. Yang, *Chem. Eng. J.* **2022**, *449*, 137790.
- [7] Y. L. Xu, R. Wang, J. Y. Wang, Y. R. Zhang, T. F. Jiao, *J. Energy Chem.* **2022**, *71*, 36–44.
- [8] Y. C. Wu, Y. J. Wang, Z. W. Wang, X. T. Li, *J. Mater. Chem. A* **2021**, *9*, 23574–23581.
- [9] H. W. Xu, J. W. Zhu, P. Y. Wang, D. Chen, C. T. Zhang, M. J. Xiao, Q. L. Ma, H. W. Bai, R. Qin, J. J. Ma, S. C. Mu, *J. Mater. Chem. A* **2021**, *9*, 24677–24685.
- [10] C. J. Lyu, J. R. Cheng, K. L. Wu, J. W. Wu, N. Wang, Z. L. Guo, P. F. Hu, W. M. Lau, J. L. Zheng, *Appl. Catal. B* **2022**, *317*, 121799.
- [11] Q. Zhang, S. H. Tang, L. H. Shen, W. X. Yang, Z. Tang, L. M. Yu, *CrystEngComm* **2021**, *23*, 4724–4731.
- [12] a) X. Y. Wang, X. B. Liu, S. Q. Wu, K. Liu, X. M. Meng, B. Li, J. P. Lai, L. Wang, S. H. Feng, *Nano Energy* **2023**, *109*, 108292; b) J. Duan, S. Chen, C. A. Ortiz-Ledon, M. Jaroniec, S. Z. Qiao, *Angew. Chem. Int. Ed.* **2020**, *59*, 8181–8186.
- [13] M. Guo, H. Y. Zhu, P. F. Wan, F. Xu, C. H. Wang, S. J. Lu, Y. F. Zhang, H. S. Fan, J. Xu, *Adv. Funct. Mater.* **2022**, *4*, 1511–1524.
- [14] W. L. Dai, M. L. Zou, C. Zhao, J. Zhang, L. G. Wang, X. S. Wang, L. X. Yang, L. Zhou, J. P. Zou, X. B. Luo, S. L. Luo, G. H. Jing, *Appl. Catal. B* **2022**, *317*, 121769.
- [15] a) N. C. Zheng, X. He, R. T. Hu, R. L. Wang, Q. Zhou, Y. K. Lian, Z. F. Hu, *Appl. Catal. B* **2022**, *307*, 121157; b) Y. N. Zhou, W. H. Hu, Y. N. Zhen, B. Dong, Y. W. Dong, R. Y. Fan, B. Liu, D. P. Liu, Y. M. Chai, *Appl. Catal. B* **2022**, *309*, 121230.
- [16] V. K. Singh, U. T. Nakate, P. Bhuyan, J. Y. Chen, D. T. Tran, S. Park, *J. Mater. Chem. A* **2022**, *10*, 9067–9079.
- [17] V. K. Singh, B. Mukherjee, S. Assa Aravindh, S. Das, *Appl. Surf. Sci.* **2023**, *609*, 155354.
- [18] S. W. Wu, S. Q. Liu, X. H. Tan, W. Y. Zhang, K. Cadien, Z. Li, *Chem. Eng. J.* **2022**, *442*, 136105.
- [19] Y. Hu, M. Guo, C. Hu, J. X. Dong, P. X. Yan, T. Taylor Isimjan, X. L. Yang, *J. Colloid Interface Sci.* **2022**, *608*, 2066–2074.
- [20] P. X. Yan, Y. J. Qin, Y. T. Yang, X. Shao, T. T. Isimjan, X. L. Yang, *Int. J. Hydrogen Energy* **2022**, *47*, 23530–23539.
- [21] B. Zhang, J. Shan, W. Wang, P. Tsiakaras, Y. Li, *Small* **2022**, *18*, 2106012.
- [22] Q. Zhao, B. B. Yang, H. W. Ren, S. H. Chen, C. H. Luo, Q. D. Li, W. Yang, K. P. Yan, *Hydrometallurgy* **2022**, *211*, 105875.
- [23] a) L. Zhou, M. F. Shao, J. B. Li, S. Jiang, M. Wei, X. Duan, *Nano Energy* **2017**, *41*, 583–590; b) B. Wei, G. C. Xu, J. C. Hei, L. Zhang, T. T. Huang, *Int. J. Hydrogen Energy* **2021**, *46*, 2225–2235.
- [24] M. Manikanta Kumar, C. R. Raj, *ACS Appl. Mater. Interfaces* **2022**, *14*, 15176–15186.
- [25] K. Zhang, J. Jia, E. D. Yang, S. P. Qi, H. Z. Tian, J. X. Chen, J. Li, Y. B. Lou, Y. Z. Guo, *Nano Energy* **2023**, *114*, 108601.
- [26] Y. Q. Liu, Z. H. Zhang, L. Zhang, Y. G. Xia, H. Q. Wang, H. Liu, S. G. Ge, J. H. Yu, *J. Mater. Chem. A* **2022**, *10*, 22125–22134.
- [27] Y. K. Sun, W. Y. Sun, L. H. Chen, A. L. Meng, G. C. Li, L. Wang, J. F. Huang, A. L. Song, Z. H. Zhang, Z. J. Li, *Nano Res.* **2022**, *16*, 228–238.
- [28] J. W. Zhu, J. Q. Chi, T. Cui, L. L. Guo, S. Q. Wu, B. Li, J. P. Lai, L. Wang, *Appl. Catal. B* **2023**, *328*, 122487.
- [29] H. Yu, L. Qi, Y. Hu, Y. Qu, P. Yan, T. T. Isimjan, X. Yang, *J. Colloid Interface Sci.* **2021**, *600*, 811–819.
- [30] a) Z. Chen, Y. Xu, D. Ding, G. Song, X. Gan, H. Li, W. Wei, J. Chen, Z. Li, Z. Gong, X. Dong, C. Zhu, N. Yang, J. Ma, R. Gao, D. Luo, S. Cong, L. Wang, Z. Zhao, Y. Cui, *Nat. Commun.* **2022**, *13*, 763; b) H. Ma, Z. Chen, Z. Wang, C. V. Singh, Q. Jiang, *Adv. Sci.* **2022**, *9*, e2105313.
- [31] a) S. Y. Xu, P. Zhang, H. Li, Z. Y. Li, Z. F. An, C. H. Chung, J. Y. Lee, J. M. Kim, P. J. Yoo, *Chem. Eng. J.* **2023**, *452*, 139461; b) Z. Wu, Y. Feng, Z. Qin, X. Han, X. Zheng, Y. Deng, W. Hu, *Small* **2022**, *18*, 2106904.
- [32] W. L. Liang, M. Y. Zhou, X. L. Li, L. J. Zhu, Z. X. Li, Y. F. Zhou, J. Chen, F. Y. Xie, H. F. Wang, N. Wang, Y. S. Jin, H. Meng, *Chem. Eng. J.* **2023**, *464*, 142671.
- [33] Z. X. Chen, J. Q. Chang, C. Liang, W. B. Wang, Y. Q. Li, Z. Q. Li, Y. Zhang, *Nano Today* **2022**, *46*, 101592.
- [34] R. Z. Zhang, L. L. Lu, Z. H. Chen, X. Zhang, B. Y. Wu, W. Shi, P. Cheng, *Chem. Eur. J.* **2022**, *28*, e202200401.
- [35] K. L. Wu, C. Y. Cao, K. R. Li, C. J. Lyu, J. R. Cheng, H. Y. Li, P. F. Hu, J. W. Wu, W. M. Lau, X. X. Zhu, P. Qian, J. L. Zheng, *Chem. Eng. J.* **2023**, *452*, 139527.
- [36] W. K. Zhao, C. Luo, Y. Lin, G. B. Wang, H. M. Chen, P. Y. Kuang, J. G. Yu, *ACS Catal.* **2022**, *12*, 5540–5548.
- [37] J. Fan, C. Fu, R. Liang, H. Lv, C. Fang, Y. Guo, W. Hao, *Small* **2022**, *18*, 2203588.
- [38] H. Li, Z. Liu, L. Wang, M. Guo, T. T. Isimjan, X. Yang, *Chem. Eur. J.* **2023**, *29*, e202203207.
- [39] Y. Bai, H. Zhang, X. Lu, L. Wang, Y. Zou, J. Miao, M. Qiao, Y. Tang, D. Zhu, *Chem. Eur. J.* **2023**, *29*, e202300205.
- [40] Z. Y. Huang, Z. Q. Liu, M. Liao, L. X. Wang, Z. Y. Luo, T. T. Isimjan, X. L. Yang, *Chem. Eng. J.* **2023**, *462*, 142281.
- [41] D. Chen, R. Lu, R. Yu, Y. Dai, H. Zhao, D. Wu, P. Wang, J. Zhu, Z. Pu, L. Chen, J. Yu, S. Mu, *Angew. Chem. Int. Ed.* **2022**, *61*, e202208642.
- [42] a) B. X. Ni, R. Chen, L. M. Wu, P. C. Sun, T. H. Chen, *Sci. China Mater.* **2021**, *64*, 1159–1172; b) X. G. Duan, J. Kang, W. J. Tian, H. Y. Zhang, S. H. Ho, Y. A. Zhu, Z. M. Ao, H. Q. Sun, S. B. Wang, *Appl. Catal. B* **2019**, *256*, 117795.
- [43] a) Y. N. Men, P. Li, J. H. Zhou, S. L. Chen, W. Luo, *Cell Rep. Phys. Sci.* **2020**, *1*, 100136; b) X. Y. Zhang, F. T. Li, Z. N. Shi, B. Dong, Y. W. Dong, Z. X. Wu, L. Wang, C. G. Liu, Y. M. Chai, *J. Colloid Interface Sci.* **2022**, *615*, 445–455.
- [44] a) G. J. Yuan, J. L. Bai, L. Zhang, X. Chen, L. L. Ren, *Appl. Catal. B* **2021**, *284*, 119693; b) X. M. Li, Q. Y. Hu, H. Y. Wang, M. Chen, X. G. Hao, Y. F. Ma, J. Liu, K. Y. Tang, A. Abudula, G. Q. Guan, *Appl. Catal. B* **2021**, *292*, 120172.
- [45] a) L. X. Wang, H. B. Yu, Z. Y. Huang, Z. Y. Luo, T. T. Isimjan, S. L. Xu, X. L. Yang, *Electrochim. Acta* **2023**, *443*, 141932; b) Z. Luo, Q. Peng, Z. Huang, L. Wang, Y. Yang, J. Dong, T. T. Isimjan, X. Yang, *J. Colloid Interface Sci.* **2022**, *629*, 111–120.
- [46] a) T. I. Singh, A. Maibam, D. C. Cha, S. Yoo, R. Babarao, S. U. Lee, S. Lee, *Adv. Sci.* **2022**, *9*, 2201311; b) Z. L. Liu, C. Yuan, F. Teng, *J. Alloys Compd.* **2019**, *781*, 460–466; c) L. X. Wang, Z. Y. Huang, H. X. Huang, S. H. Zhong, M. L. Huang, T. T. Isimjan, X. L. Yang, *Electrochim. Acta* **2022**, *404*, 139598.

Manuscript received: May 14, 2023

Accepted manuscript online: July 12, 2023

Version of record online: September 4, 2023